

<https://doi.org/10.1038/s41535-024-00700-z>

Probing p -wave superconductivity in UTe_2 via point-contact junctions



Hyeok Yoon¹, Yun Suk Eo¹, Jihun Park^{1,2}, Jarryd A. Horn¹, Ryan G. Dorman¹, Shanta R. Saha¹, Ian M. Hayes¹, Ichiro Takeuchi^{1,2}, Philip M. R. Brydon³ & Johnpierre Paglione^{1,4} ✉

Uranium ditelluride (UTe_2) is the strongest contender to date for a p -wave superconductor in bulk form. Here we perform a spectroscopic study of the ambient pressure superconducting phase of UTe_2 , measuring conductance through point-contact junctions formed by metallic contacts on different crystalline facets down to 250 mK and up to 18 T. Fitting a range of qualitatively varying spectra with a Blonder-Tinkham-Klapwijk (BTK) model for p -wave pairing, we can extract gap amplitude and interface barrier strength for each junction. We find good agreement with the data for a dominant p_y -wave gap function with amplitude 0.26 ± 0.06 meV. Our work provides spectroscopic evidence for a gap structure consistent with the proposed spin-triplet pairing in the superconducting state of UTe_2 .

The recent discovery of spin-triplet superconductivity in UTe_2 ¹ has raised the possibility of realizing the technological dream of odd-parity pairing with non-trivial topology in a natural solid state material. The strongest signatures of triplet pairing in UTe_2 include upper critical fields greatly exceeding the Pauli limit for each crystal orientation¹, re-entrant superconductivity in ultra-high magnetic fields², and near absence of changes in the NMR Knight shift below the superconducting transition temperature^{3,4}. Together with the observation of chiral in-gap states revealed by scanning tunneling microscopy (STM) studies⁵ and a normal surface fluid identified in microwave impedance measurements⁶, these ingredients provide strong evidence for the non-trivial topological nature of superconductivity in UTe_2 .

The intrinsic symmetry of the superconducting order parameter, which requires identification in order to understand both the pairing mechanism as well as the nature of topological excitations, belongs to the irreducible representation of the point group of the material's crystal structure (D_{2h}). Assuming spin-triplet pairing, the orbital component of the order parameter should be odd, constraining the possible candidates to A_u (full-gap), B_{iu} ($i = 1, 2, 3$; point-nodes), and their combinations^{7,8}. Experimental studies on the first generation of UTe_2 crystals proposed a multi-component order parameter, i.e., $B_{3u} + iB_{2u}$ or $A_u + iB_{1u}$, based on the observation of nodal excitations in thermal transport⁹, broken time-reversal symmetry (TRS) in polar Kerr effect experiments and two distinct superconducting transitions in specific heat¹⁰. However, later generation materials with higher T_c values appear to have only a single thermodynamic transition, a small but finite Knight shift^{3,4}, and an apparent lack of TRS breaking¹¹, raising the possibility that a two-component order parameter is not an intrinsic property of UTe_2 ^{12–14}.

Ultimately, the lack of a jump in elastic shear moduli in both generations of materials¹⁵ points conclusively to a single-component order parameter, but is still inconsistent with the observation a quadratic temperature dependence of magnetic penetration depth for all crystallographic directions^{9,16}.

Spectroscopic studies have historically been very decisive in determining superconducting order parameter symmetry. In UTe_2 , STM studies by four independent groups have successfully probed the cleaved surface and the superconducting gap at the Fermi level^{5,17–21}, but have only studied the easy-cleavage plane (011)^{5,17–19} and the (001) surface²¹. More important, studies of the gap structure by STM have been hindered by the abundance of in-gap states that fill in a large fraction of the differential conductance, which remains a mystery but is likely affected by the presence of surface states such as charge^{17,18} and pair-density wave orders¹⁹, as well as the anomalous non-superconducting fluid at the surface⁶.

An alternative approach to studying the directional nature of the superconducting order parameter is to fabricate normal-metal/(insulator)/superconductor (N-(I)-S) junctions in which facets are defined by oriented polishing of bulk single crystals, and performing spectroscopic tunneling experiments. However, to date the realization of a functional device has been a challenge due to the lack of understanding of surface oxidation and interface quality. In this study, we present the successful measurement of energy spectra in Au/Ti/ UTe_2 planar junctions formed on two different facet orientations by utilizing the surface oxidation layer of UTe_2 . The observed conductance spectra are well described by a p -wave BTK model for tunneling into triplet superconductors and suggest a dominant p_y -wave symmetry as the most plausible order parameter for the ambient pressure superconductivity of UTe_2 .

¹Department of Physics, Maryland Quantum Materials Center, University of Maryland, College Park, MD, USA. ²Department of Materials Science and Engineering, University of Maryland, College Park, MD, USA. ³Department of physics and MacDiarmid Institute for Advanced Materials and Nanotechnology, University of Otago, Dunedin, New Zealand. ⁴Canadian Institute for Advanced Research, Toronto, ON, Canada. ✉e-mail: paglione@umd.edu

Results and discussion

Native oxide in UTe_2 point-contact junctions

Our point-contact junctions incorporate the native oxide of UTe_2 that forms upon exposure to air. The baking process of photoresist during the fabrication further enhances the surface oxidation, making its thickness more than tens of nanometers (see SM, section I). Despite the thick oxidation layer, our junction resistances maintain low ($R_c < 10 \Omega$) values at low temperatures. Considering the nature of the oxidation layer, it is likely that there exists metallic shorts through the layer that form leaking paths in large-size N-I-S planar junctions that decrease the effective size of junctions, thereby suppressing inelastic electron scattering across the junctions (Fig. 1a). In this ballistic regime, the spectra can reflect the energy density of states of the sample layer as shown in many other cases^{22–27}. Despite the inability to form a proper tunnel barrier, we can therefore utilize this configuration to perform point-contact spectroscopy.

Differential conductance measurements for two different orientations

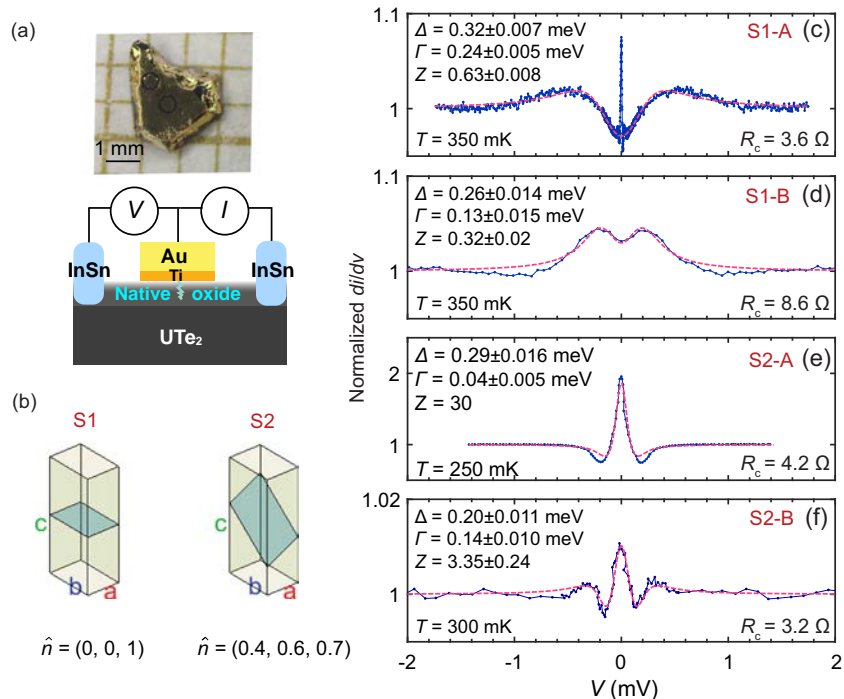
Figures 1 and 2 show the differential conductance spectra across the junctions (S1-A, S1-B, S2-A, S2-B) at the base temperature and their temperature evolution. Here, S1 and S2 label the crystals, and A and B label the junctions. For example, S1-A is the junction A fabricated on the crystal S1. S1-A and S1-B are fabricated on the same facet (001) of the crystal S1, and S2-A and S2-B are created on the opposing faces of crystal S2, which run parallel to each other. The surface normal vector of S2 facet is $\hat{n} = [0.4, 0.6, 0.7]$ (see SM, section II). Figure 1b presents a schematic of the facets of the junctions on samples S1 and S2, demonstrating the different orientation of the conductance measurements for each sample. In Fig. 1c–f, spectra are normalized to the normal-state spectra above T_c . As shown in Fig. 2, features in the differential conductance spectra are developed below the superconducting transition temperature and the upper critical field for all junctions, and the details of each spectra are described below.

All junctions presented in this study exhibit spectral features consistent with a gap opening of UTe_2 . Sample S1-A exhibits a dip feature at an energy close to the expected superconducting gap energy $\Delta = 0.25$ meV, estimated from the weak-coupling BCS theory (i.e., $2\Delta/k_B T_c = 3.56$), with shoulders reminiscent of coherence peaks in the superconducting density of states.

However, this sample also exhibits a prominent peak at zero-bias, as shown in Fig. 1c. The coherence peaks vanish in the vicinity of T_c , and the parabolic background remains in the normal state spectra. On the other hand, when the magnetic field is applied in-plane (15° off from the b -axis), the coherence peak disappears. We note that determining when exactly the coherence peaks disappear is not clear since the background dip structure is deeper and remains even beyond $\mu_0 H_{c2} = 11.4$ T, in contrast to the normal-state spectra above T_c . While the zero-bias peak (ZBP) is a very interesting feature that could possibly be associated with zero-energy Andreev states which occur in a topological superconductor, we first note that its energy width is narrower than the minimum broadening possible due to the thermal smearing of the spectra; the peak width is $\sim 10 \mu\text{eV}$ while $k_B T = 25 \mu\text{eV}$ at $T = 300$ mK. Out of many possible reasons for the ZBP in the differential conductance²⁸, to our knowledge the only source immune to thermal broadening is from a Josephson supercurrent across the junction. This is an interesting aspect of sample S1-A that was not reproduced in other junctions, and may be an indication of a tunneling phenomenon. However, it is important to note that our Au/Ti counter-electrode is not superconducting in the range where the zero-bias peak is observed (i.e., up to 1 K), raising the question of what component plays the role of a superconducting electrode in such a SNS or SIS Josephson configuration (see SM, section IV).

Sample S1-B, which is a separate junction on the same crystal facet as S1-A, exhibits a different shape consisting of a small dip imposed on a broad conductance enhancement (Fig. 1d). In addition, we also see a weak dip in conductance at energies higher than the low-energy enhancement. This combined peak-dip structure is often observed in the thermal regime of contacts and can be explained by the influence of the critical current, causing the system to transition into a high-resistance state before the local superconductivity is suppressed^{29–32}. In this case, the small dip represents the energy spectra imposed on the broad peak due to the superconductivity. The energy scale of this dip feature matches the superconducting gap size Δ (~ 0.2 meV) of UTe_2 , which is consistent with this scenario. Note that the peak-dip feature has also been observed in other materials such as Pt-Sr₂RuO₄ point-contact junctions, but was explained in a different manner by incorporating a phenomenological transmission cone instead of attributing the structure to critical current effects³³. This model suggests that it could be also feasible to fit our S1-B junction without taking the critical current into account.

Fig. 1 | Differential conductance spectra of UTe_2 junctions at 250–350 mK. **a** Schematic of point-contact devices fabricated using single-crystal samples of UTe_2 . **b** Graphical representation of facet directions of samples S1 and S2. **c–f** Normalized differential conductance (blue) and fits (magenta) using a p -wave BTK model as described in the main text. Obtained fit parameter values for gap energy Δ , scattering rate Γ , impedance Z , and temperature T are noted. Here, T is fixed to the experimentally measured temperature, and Z is a fitting parameter except for S2-A. Z is set to 30 for S2-A for convenience, since there is very little variation in the spectra with increasing Z upon entering the tunneling regime. Each junction resistance is shown in the figure.



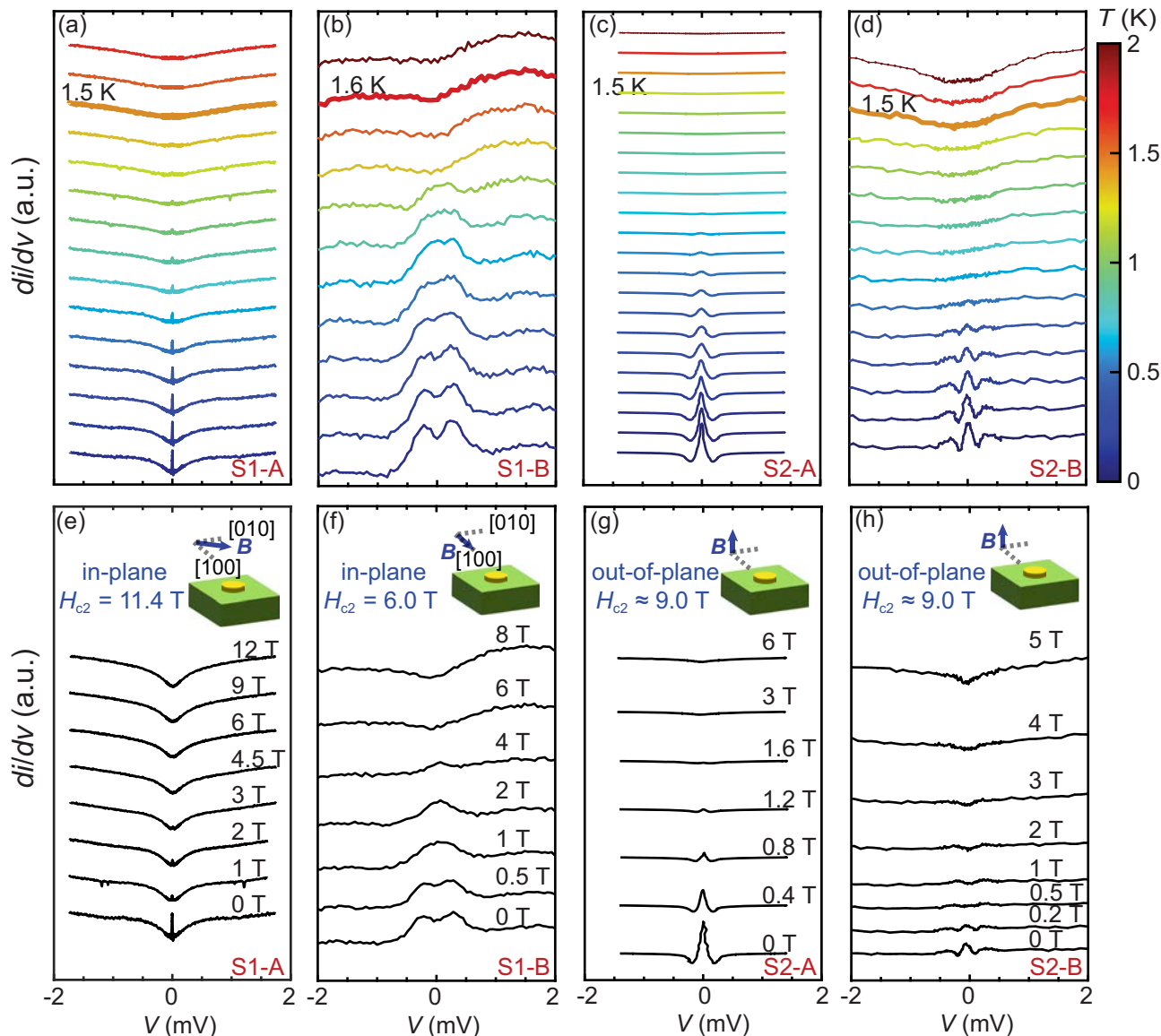


Fig. 2 | Temperature and magnetic field dependence of the differential conductance of UTe₂ junctions. a–d Zero-field differential conductance di/dv measured at fixed temperatures between 0.3 K and 2 K. For each panel, the $T = 1.5$ K or 1.6 K data are labeled to denote the resistive transition temperature. e–h Magnetic field dependence of di/dv measured at 350 mK for S1 and 250 mK for S2. For S1-A

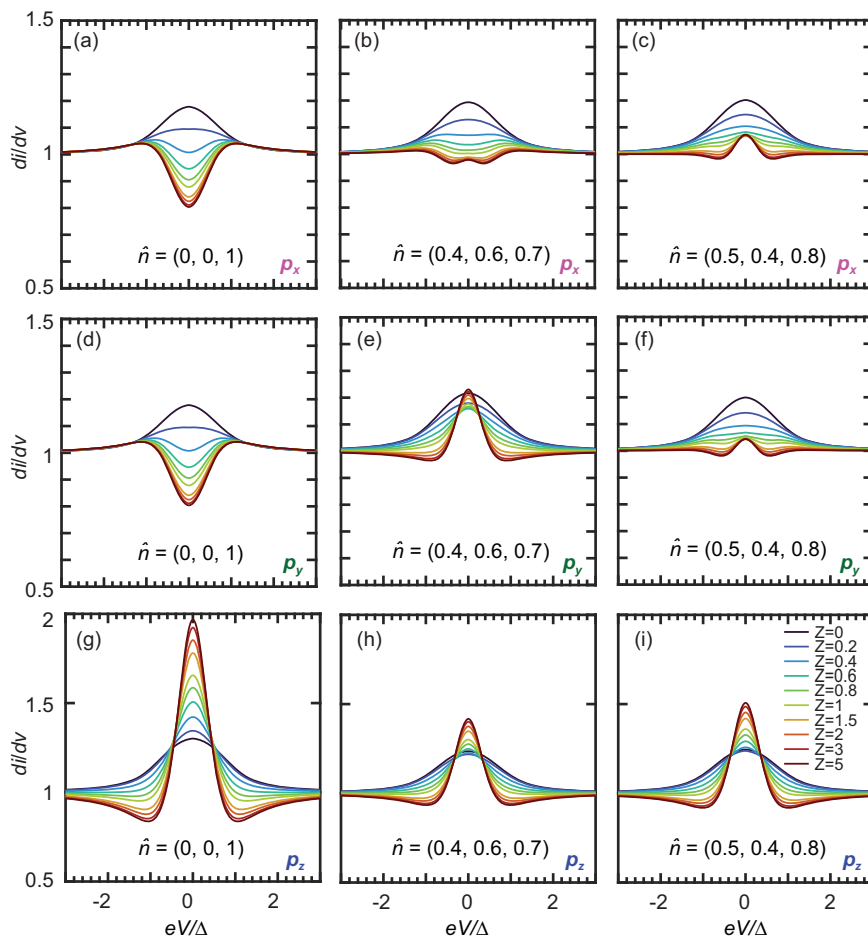
and S1-B, the magnetic field is applied in-plane, and the upper critical field is obtained from the independently measured resistive transition. For S2-A and S2-B, the magnetic field is applied out-of-plane, and the upper critical field is estimated using the orientation of facets and the known angle dependence (see SM, section III).

Sample S2-A exhibits a peak-dip structure as well, but with a very sharp ZBP and dips on either side at higher energies. The strong ZBP has amplitude nearly twice as large as the background as shown in Fig. 1(e), and is often seen in point-contact junctions and explained via various origins. First, the ZBP may result from the prevalent Andreev reflection. However, the distinctive dip outside this ZBP can not be explained solely with Andreev reflection. It is possible that the peak-dip structure originates from the addition of tunneling and Andreev reflections in the presence of a proximitized normal layer³⁴. However, we rule out this case because the energy scale of the peak is close to the UTe₂ gap, unlike the expectation from this scenario. It is also possible that the ZBP can appear in *s*-wave/ferromagnet interface, but we exclude this scenario because our junctions do not consist of such ingredients³⁵. Second, the peak-and-dip structure can be interpreted as the effect of critical current, as discussed for S1-B. Nonetheless, we exclude this scenario because the background of the spectra is T independent when the ZBP appears, whereas the transport-like conduction is expected to show the resistivity decreasing quadratically in temperature

(see SM, section V). In addition, if the dip and ZBP structure arises from the critical current, the dip should be spike-like and its position should shift to the center as T increases, as reflecting the features of the critical current. In contrast, the width of the ZBP in our spectra does not change significantly with increasing T . Also, in our case, the peak intensity is sharply suppressed as T increases, contrasting with the binary character of the resistive transition. Hence, we attribute the ZBP to the existence of surface Andreev-bound states often observed in the tunneling limit. This ZBP originates from the interference of the transmitted electron-like quasi-particle and hole-like quasi-particle experiencing the phase difference of the pair potential^{36,37}. This constructive interference can be induced when the electrons are injected along the nodal direction of *d*-wave superconductors³⁸ or in the *p*-wave topological superconductors^{39,40}.

Finally, for sample S2-B, the spectrum has similar features to both S1-B and S2-A, but with much smaller ZBP intensity as compared to S2-A as shown in Fig. 1f. The varying features in the four spectra present differing behavior that are actually useful for identifying distinct responses due to gap

Fig. 3 | BTK simulation of normalized differential conductance using p -wave model. Simulated conductance spectra are presented for junctions oriented along different facets of the orthorhombic crystal structure, plotted as a function of interface barrier strength Z (color scale) ranging between 0 (blue) and 5 (red). **a–i** show the BTK simulation with p_x, p_y, p_z respectively. **a, d, g** are BTK simulation at the facet $\hat{n} = [0, 0, 1]$. **b, e, h** are BTK simulation at the facet $\hat{n} = [0.4, 0.6, 0.7]$. **c, f, i** are BTK simulations at the facet $\hat{n} = [0.5, 0.4, 0.8]$. All spectra are plotted with fixed parameters $k_B T = 0.1\Delta$ and $\Gamma = 0.4\Delta$.



structure, and can be reasonably well modeled by variations of junction parameters using a p -wave gap scenario as explained below.

Fitting with the p -wave BTK model

To model these conductance spectra, we have utilized a generalization of the BTK theory⁴¹ for tunneling into triplet superconductors⁴², calculating the conductance according to the formula

$$\frac{dI}{dV} = \sigma_N \int_{-\infty}^{\infty} \sigma_{\text{BTK}}(E + i\Gamma) \left[-\frac{\partial f(E + eV)}{\partial E} \right] dE \quad (1)$$

where σ_N is the normal-state tunneling conductance, $\sigma_{\text{BTK}}(E)$ is the normalized BTK conductance, $f(E)$ is the Fermi function, and Γ is a phenomenological broadening parameter. Details of the calculation are presented in the supplemental material (see SM, section VI). As discussed earlier, a number of previous experiments point to a triplet order parameter in UTe_2 , and so we assume a p -wave triplet model to fit the data. We also find that p -wave symmetry gives a better fit than s -wave and d -wave singlet states, as the p -wave fit results in the smallest Γ/Δ value. (see SM, section VII). The orthorhombic crystal symmetry of UTe_2 places few constraints on the structure of the triplet pairing states in each irrep: even upon restricting to p -wave gap symmetry, a general pairing state has two (B_{1u} , $i = 1, 2, 3$) or three (A_u) independent gap components. Since our experimental results are unable to distinguish between single-component (non-chiral) and multi-component (chiral) gaps due to the limited energy resolution, we assume that the pairing state preserves TRS to keep our task manageable. Our fitting parameters hence consist of the relative strength of the different p -wave components, the overall gap amplitude Δ , the interface barrier strength Z , and Γ . We find that the data is best fit by a pairing state with a dominant p_y -

wave gap component. In other words, our spectra is best fitted with B_{1u} , B_{3u} and A_u , which all include a p_y component. We are not able to further refine the gap structure because of the low energy resolution resulting from the thermal and intrinsic broadening. Due to this uncertainty, here we present fits to the data with a purely p_y -wave gap function $\Delta(\mathbf{k}) = \Delta_0 k_y/k_F$ with zero-temperature gap amplitude in the range 0.2 to 0.35 meV. The obtained gap size is consistent with values of $\Delta = \pm 0.25$ meV obtained by spectroscopic STM experiments on the [011] crystalline surface⁵. We stress that we cannot exclude the presence of other symmetry-allowed p -wave gap components, which are required for consistency with thermodynamic measurements indicating point nodes, but our analysis suggests that they are smaller than the p_y -wave component.

The ZBP offers an important clue to gap structure of an unconventional superconductor: a pronounced ZBP typically indicates zero-energy surface Andreev bound states, which occur when the superconducting gap changes sign upon reversing the momentum component normal to the surface; on the other hand, the absence of the ZBP is consistent with a gap which does not change sign upon this reversal. For a p -wave superconductor the differential conductance is anisotropic; in particular, the presence or absence of a ZBP at a given surface is characteristic of different p -wave gaps. This argument is approximately robust to the presence of subdominant gap components, as discussed in the supplemental material (see SM, section VI). To visualize this concept, Fig. 3 demonstrates the normalized differential conductance spectra for the facets of our samples, simulated from the BTK theory using a p -wave model. As shown in Fig. 3a, d, g, the gap-like feature around zero-bias in the S1-A and S1-B conductance data ($\hat{n} = [0, 0, 1]$) is thus not consistent with a dominant p_z -wave gap component, and indeed can be reasonably fit by a purely p_x - or p_y -wave gap.

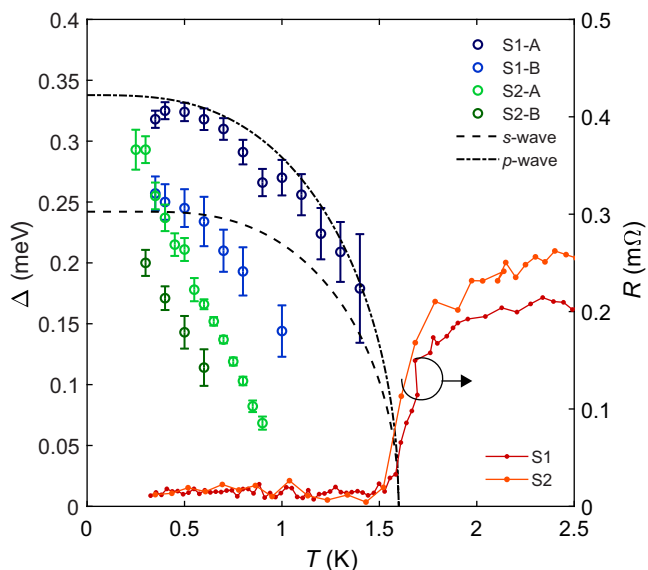


Fig. 4 | Extracted Superconducting energy gap magnitudes. Circles represent the gap sizes extracted from the p -wave BTK fits. The uncertainty is defined by the 95% confidence interval for the fit. The dashed and dotted curves are the simulated temperature dependence of Δ for s -wave and p -wave models, respectively, with T_c fixed at 1.6 K. The red and orange curves, measured in S1 and S2, respectively, demonstrate the superconducting transition measured by four-probe resistance using ohmic contacts as current leads and point-contacts for voltage leads.

On the other hand, as shown in Fig. 3b, e, h, a purely p_z - or p_y -wave state gives the best fit to the sharp ZBP in the S2-A data, consistent with the surface normal lying 23° away from the y - z plane. We note that the prominence and height of the peak is enhanced by reducing the broadening Γ , which in Fig. 3 is several times larger than in our fit to the S2-A data. Since the S1 data excludes a dominant p_z -wave component, this implies that the gap is predominantly p_y -wave in character.

The S2-B case is least consistent with a purely p_y -wave gap, and a better fit is obtained for a p_x -wave state. Although this is hard to reconcile with the S2-A data for nominally the same surface normal, assuming a slight misalignment of the surface normal compared to the S2-A surface yields an excellent fit to a purely p_y -wave gap. Specifically, best agreement is obtained for an approximately 10° misalignment ($\hat{n} = [0.5, 0.4, 0.8]$), which is shown in Fig. 3c, f, i. This degree of misalignment is experimentally possible since S2-B is fabricated on the other side of S2-A, possibly making the two facets not exactly parallel.

The variation of the fitted gap amplitude with temperature is shown in Fig. 4. The S1-A data follows rather closely the weak-coupling temperature dependence of a p -wave pairing state with $T_c = 1.6$ K; the S1-B data shows a similar variation albeit with somewhat lower critical temperature. In contrast, the S2-A and S2-B data show an approximately linear decline in the gap as a function of temperature, extrapolating to zero for $T_c \leq 1$ K, which suggests a lower T_c at the surface. The lower T_c for S1-B, S2-A, and S2-B could originate from the surface degradation. However, weakened superconductivity at the degraded surface is necessarily inherited from the bulk state, so it is unlikely to exhibit a different pairing symmetry. Additionally, we do not believe the lower T_c results from inhomogeneity caused by local impurities present in the low-quality samples, as the probed areas are much larger than the size of such impurities. Therefore, a similar study on high-quality samples would likely encounter the same surface degradation issues and would not differ significantly from the current study.

Our theoretical analysis has utilized a number of standard simplifying assumptions. In particular, we treat the Fermi surface in both the lead and superconductor as spherical with the same Fermi wavevector and effective mass. Although this is inconsistent with the quasi-2D Fermi surface and significant orthorhombic anisotropy in normal-state resistivity in UTe_2 ,

accurately accounting for the band structure typically does not introduce significant quantitative changes in the BTK theory predictions⁴³. However, the unexpected linear T -dependence of the gaps measured at the S2 surfaces may indicate a breakdown of our BTK theory. In particular, we have neglected the variation of the gap near the surface of the material, which could be significant at the S2 surfaces of our proposed p_y -wave state. Accounting for this might alter the quantitative values of our fit parameters but is not expected to qualitatively alter our conclusions; in particular, the relation between the ZBP and the gap symmetry can be formulated in terms of topological invariants⁴⁴, making this feature somewhat immune to details of the surface.

In summary, we have presented point-contact spectra of the superconducting state of UTe_2 using four distinct junctions fabricated by depositing Ti/Au metal contacts on the native oxide surface of UTe_2 single crystals with two different facet orientations. By fitting conductance spectra measured with currents directed along both ($\hat{n} = [0, 0, 1]$) and ($\hat{n} = [0.4, 0.6, 0.7]$), we are able to model the data with a simple p -wave BTK model, extracting gap amplitude and constraining the gap structure. All junctions exhibit spectroscopic features that close at the superconducting transition temperature and upper critical field of UTe_2 , with energies in 0.26 ± 0.06 meV consistent with energy scales observed in scanning tunneling spectroscopy and derived from thermodynamic quantities. Upon careful examination of a p -wave BTK model, we conclude that a gap with a dominant p_y -wave component is the most consistent with our data. Our study demonstrates the potential of performing electronic spectroscopy in UTe_2 in a stable device with choice of crystalline facet direction and external environment, opening the door to further studies of the multiple superconducting phases of UTe_2 , including the re-entrant and field-polarized states.

Methods

Single crystals of UTe_2 were grown by the chemical vapor transport method⁴⁵, yielding samples with a transition temperature $T_c = 1.6$ K. Orientation of crystal facets was determined using the anisotropy in magnetic susceptibility. Facets on two samples (S1 with (001) facet, and S2 with facet normal vector $\hat{n} = [0.4, 0.6, 0.7]$) were polished using aluminum oxide lapping films, and metal contacts were fabricated using Au thin films deposited by evaporation. 3–5 nm of Ti is deposited prior to Au to enhance adhesion to UTe_2 . S1 and S2 were patterned by conventional lithography, with details of the fabrication process and dimensional parameters described in SM, section VIII-A and B. During fabrication, samples are heated at 100°C for 1 min for baking photoresist and additionally heated at 100 – 120°C for 2–3 min to adhere glue to a cover glass. In-Sn solder was used to make ohmic contacts to samples (see SM, section VIII-C). The final device structure is shown in Fig. 1a. For the electrical measurements, transport and differential conductance measurements were performed using a ^3He commercial probe with base temperature of around 300 mK.

Data availability

The data that support the findings of this study are available from the corresponding author upon reasonable request.

Code availability

The underlying code for this study is not publicly available but may be made available to qualified researchers on reasonable request from the corresponding author.

Received: 1 April 2024; Accepted: 22 October 2024;

Published online: 15 November 2024

References

- Ran, S. et al. Nearly ferromagnetic spin-triplet superconductivity. *Science* **365**, 684–687 (2019).
- Ran, S. et al. Extreme magnetic field-boosted superconductivity. *Nat. Phys.* **15**, 1250–1254 (2019).

3. Nakamine, G. et al. Superconducting properties of heavy fermion UTe_2 revealed by ^{125}Te -nuclear magnetic resonance. *J. Phys. Soc. Jpn.* **88**, 113703 (2019).
4. Matsumura, H. et al. Large reduction in the a-axis Knight shift on UTe_2 with $T_c = 2.1$ K. *J. Phys. Soc. Jpn.* **92**, 063701 (2023).
5. Jiao, L. et al. Chiral superconductivity in heavy-fermion metal UTe_2 . *Nature* **579**, 523–527 (2020).
6. Bae, S. et al. Anomalous normal fluid response in a chiral superconductor UTe_2 . *Nat. Commun.* **12**, 2644 (2021).
7. Shishidou, T., Suh, H. G., Brydon, P. M. R., Weinert, M. & Agterberg, D. F. Topological band and superconductivity in UTe_2 . *Phys. Rev. B* **103**, 104504 (2021).
8. Ishizuka, J., Sumita, S., Daido, A. & Yanase, Y. Insulator-metal transition and topological superconductivity in UTe_2 from a first-principles calculation. *Phys. Rev. Lett.* **123**, 217001 (2019).
9. Metz, T. et al. Point-node gap structure of the spin-triplet superconductor UTe_2 . *Phys. Rev. B* **100**, 220504 (2019).
10. Hayes, I. M. et al. Multicomponent superconducting order parameter in UTe_2 . *Science* **373**, 797–801 (2021).
11. Ajeesh, M. O. et al. Fate of time-reversal symmetry breaking in UTe_2 . *Phys. Rev. X* **13**, 041019 (2023).
12. Thomas, S. M. et al. Spatially inhomogeneous superconductivity in UTe_2 . *Phys. Rev. B* **104**, 224501 (2021).
13. Rosa, P. F. S. et al. Single thermodynamic transition at 2 K in superconducting UTe_2 single crystals. *Commun. Mater.* **3**, 33 (2022).
14. Sakai, H. et al. Single crystal growth of superconducting UTe_2 by molten salt flux method. *Phys. Rev. Mater.* **6**, 073401 (2022).
15. Theuss, F. et al. Single-component superconductivity in UTe_2 at ambient pressure. *Nat. Phys.* **20**, 1124–1130 (2024).
16. Ishihara, K. et al. Chiral superconductivity in UTe_2 probed by anisotropic low-energy excitations. *Nat. Commun.* **14**, 2966 (2023).
17. Aishwarya, A. et al. “Melting of the charge density wave by generation of pairs of topological defects in UTe_2 ”, *Nat. Phys.* **20**, 964 (2024).
18. Aishwarya, A. et al. Magnetic-field-sensitive charge density waves in the superconductor UTe_2 . *Nature* **618**, 928–933 (2023).
19. Gu, Q. et al. Detection of a pair density wave state in UTe_2 . *Nature* **618**, 921–927 (2023).
20. LaFleur, A. et al. Inhomogeneous high temperature melting and decoupling of charge density waves in spin-triplet superconductor UTe_2 . *Nat. Commun.* **15**, 4456 (2024).
21. Hu, Y. et al. Scanning tunneling microscope study of the unconventional superconducting state in UTe_2 . APS March Meeting, a61.00005 (2022).
22. Yanson, I. Nonlinear effects in the electric conductivity of point junctions and electron-phonon interaction in normal metals. *J. Exp. Theor. Phys.* **39**, 506–513 (1974).
23. Naidyuk, Y. G. & Yanson, I. K. *Point-contact Spectroscopy 2–3* (Springer, 2005).
24. Hwang, I. et al. A new simple method for point contact Andreev reflection (PCAR) using a self-aligned atomic filament in transition-metal oxides. *Nanoscale* **7**, 8531–8535 (2015).
25. Srikanth, H. & Raychaudhuri, A. K. Microshort-to-tunneling transition in $Au-YBa_2Cu_3O_{7-\delta}$ single-crystal point contacts. *Phys. Rev. B* **45**, 383–388 (1992).
26. Dvoranová, M. et al. Point contact spectroscopy of superconductors via nanometer scale point contacts formed by resistive switching. *AIP Adv.* **8**, 125217 (2018).
27. Hagiwara, T., Mizuno, O. & Tanaka, S. Electron tunneling through $Te-TeO_2-Pb$ junctions. *J. Phys. Soc. Jpn.* **34**, 973–982 (1973).
28. Kuerten, L. et al. In-gap states in superconducting $LaAlO_3-SrTiO_3$ interfaces observed by tunneling spectroscopy. *Phys. Rev. B* **96**, 014513 (2017).
29. Kumar, R. & Sheet, G. Nonballistic transport characteristics of superconducting point contacts. *Phys. Rev. B* **104**, 094525 (2021).
30. Sheet, G., Mukhopadhyay, S. & Raychaudhuri, P. Role of critical current on the point-contact andreev reflection spectra between a normal metal and a superconductor. *Phys. Rev. B* **69**, 134507 (2004).
31. Aggarwal, L. et al. Unconventional superconductivity at mesoscopic point contacts on the 3D dirac semimetal Cd_3As_2 . *Nat. Mater.* **15**, 32–37 (2016).
32. Aggarwal, L. et al. Mesoscopic superconductivity and high spin polarization coexisting at metallic point contacts on weyl semimetal $TaAs$. *Nat. Commun.* **8**, 13974 (2019).
33. Laube, F., Goll, G., Löhneysen, H. V., Fogelström, M. & Lichtenberg, F. Spin-triplet superconductivity in Sr_2RuO_4 probed by andreev reflection. *Phys. Rev. Lett.* **84**, 1595–1598 (2000).
34. Strijkers, G. J., Ji, Y., Yang, F. Y., Chien, C. L. & Byers, J. M. Andreev reflections at metal/superconductor point contacts: measurement and analysis. *Phys. Rev. B* **63**, 104510 (2001).
35. Usman, I. T. M. et al. Evidence for spin mixing in holmium thin film and crystal samples. *Phys. Rev. B* **83**, 144518 (2011).
36. Hu, C. -R. Midgap surface states as a novel signature for $d_{x^2-y^2}$ -wave superconductivity. *Phys. Rev. Lett.* **72**, 1526–1529 (1994).
37. Tanaka, Y. & Kashiwaya, S. Theory of tunneling spectroscopy of d -wave superconductors. *Phys. Rev. Lett.* **74**, 3451–3454 (1995).
38. Daghero, D. et al. Strong-coupling d -wave superconductivity in $PuCoGa_5$ probed by point-contact spectroscopy. *Nat. Commun.* **786**, 786 (2012).
39. Sasaki, S. et al. Topological superconductivity in $Cu_xBi_2Se_3$. *Phys. Rev. Lett.* **107**, 217001 (2011).
40. Zhu, W. et al. Intrinsic surface p -wave superconductivity in layered $AuSn_4$. *Nat. Commun.* **14**, 7012 (2023).
41. Blonder, G. E., Tinkham, M. & Klapwijk, T. M. Transition from metallic to tunneling regimes in superconducting microconstrictions: Excess current, charge imbalance, and supercurrent conversion. *Phys. Rev. B* **25**, 4515–4532 (1982).
42. Yamashiro, M., Tanaka, Y. & Kashiwaya, S. Theory of tunneling spectroscopy in superconducting Sr_2RuO_4 . *Phys. Rev. B* **56**, 7847–7850 (1997).
43. Daghero, D. & Gonnelli, R. S. Probing multiband superconductivity by point-contact spectroscopy. *Supercond. Sci. Technol.* **23**, 043001 (2010).
44. Schnyder, A. P. & Brydon, P. M. R. Topological surface states in nodal superconductors. *J. Phys.: Condens. Matter* **27**, 243201 (2015).
45. Ran, S. et al. Comparison of two different synthesis methods of single crystals of superconducting uranium ditelluride. *J. Vis. Exp.* **173**, e62563 (2021).

Acknowledgements

We acknowledge useful discussions with D. F. Agterberg, V. Madhavan, and A. R. Hight Walker. Research at the University of Maryland was supported by the U.S. Department of Energy Award No. DE-SC-0019154 (sample characterization), the Air Force Office of Scientific Research under Grant No. FA9950-22-1-0023 (spectroscopic experiments), the Gordon and Betty Moore Foundation’s EPIQS Initiative through Grant No. GBMF9071 (materials synthesis), and the Maryland Quantum Materials Center. S.R.S. acknowledges support from the National Institute of Standards and Technology Cooperative Agreement 70NANB17H301. P.M.R.B. was supported by the Marsden Fund Council from Government funding, managed by Royal Society Te Apārangi, Contract No. UOO1836.

Author contributions

H.Y. and J.P. (J.Paglione) conceived and designed the experiments. S.R.S. and I.M.H. synthesized single crystals. H.Y. and R.G.D. characterized the orientations of single crystals. H.Y. and Y.S.E. fabricated samples to make point-contact junctions. H.Y., Y.S.E., and J.A.H. performed the electrical measurements. H.Y. and J.P. (J.Park) characterized the surface oxidation of the samples. P.M.R.B. provides the theoretical modeling and fitting of data.

H.Y., I.T., P.M.R.B., J.P. (J.Paglione) wrote the paper. All authors read and approved the final manuscript.

Competing interests

The authors declare no competing interests.

Additional information

Supplementary information The online version contains supplementary material available at

<https://doi.org/10.1038/s41535-024-00700-z>.

Correspondence and requests for materials should be addressed to Johnpierre Paglione.

Reprints and permissions information is available at <http://www.nature.com/reprints>

Publisher's note Springer Nature remains neutral with regard to jurisdictional claims in published maps and institutional affiliations.

Open Access This article is licensed under a Creative Commons Attribution-NonCommercial-NoDerivatives 4.0 International License, which permits any non-commercial use, sharing, distribution and reproduction in any medium or format, as long as you give appropriate credit to the original author(s) and the source, provide a link to the Creative Commons licence, and indicate if you modified the licensed material. You do not have permission under this licence to share adapted material derived from this article or parts of it. The images or other third party material in this article are included in the article's Creative Commons licence, unless indicated otherwise in a credit line to the material. If material is not included in the article's Creative Commons licence and your intended use is not permitted by statutory regulation or exceeds the permitted use, you will need to obtain permission directly from the copyright holder. To view a copy of this licence, visit <http://creativecommons.org/licenses/by-nc-nd/4.0/>.

© The Author(s) 2024

Supplementary Materials for Probing p -wave superconductivity in UTe_2 via point-contact junctions

Hyeok Yoon, Yun Suk Eo, Jihun Park, Jarryd A. Horn, Ryan G. Dorman,
Shanta R. Saha, Ian M. Hayes, Ichiro Takeuchi, Philip M. R. Brydon,
Johnpierre Paglione

Correspondence to: paglione@umd.edu

This PDF file includes:

Figs. S1 - S12

Captions for Figs. S1 - S12

Table S1, S2

Captions for Table S1, S2

I. Surface oxidation in UTe₂

We use Raman spectroscopy and spectroscopic ellipsometry to understand the interface of UTe₂ junctions in this study. First, Raman spectroscopy shows that the heat treatment during the sample fabrication process induces more profound oxidation than the ambient conditions. To measure the Raman peaks in the intrinsic UTe₂, the bulk sample was cleaved right before the measurement. The intrinsic UTe₂ has a Raman-active mode around 155 cm⁻¹, as shown in Fig. S1(a). After 48 hrs in air, the new peaks at 124 and 142 cm⁻¹ appear in addition to the original peaks, as shown in Fig. S1(b). These modes can be either α -TeO₂ or elemental Te, both of which are the semiconductors [1]. On the other hand, when the cleaved sample is exposed to heat at 100 °C for 5 minutes in air, which is the similar conditions to the sample fabrication process, the oxidation peak becomes more pronounced.

Furthermore, we estimate the thickness of the oxide layer of our sample using spectroscopic ellipsometry. Figure S2 shows the inverse tangential component of the amplitude ratio Φ at the left-axis and the phase shift δ at the right-axis. Assuming the oxide layer added on the bare surface of UTe₂ after heat-treatment is uniform, we use a bi-layer model which uses a bottom layer as a bare UTe₂ spectra (blue) to fit the heat-treated data (red). The best-fits occurs when the thickness of oxide layer is 85 nm.

For Raman spectroscopy, LabRam Aramis from Horiba Jobi Yvon was used with 532 nm source wavelength, 11 μ W power and 200 second exposure time for the measurement. We confirmed that this beam condition does not damage the samples by checking the reproducibility in the spectra in identical conditions. For ellipsometry, M-2000 spectroscopic ellipsometer from J.A. Wollam Co. was used for the measurement, and CompleteEASE software was used for fitting.

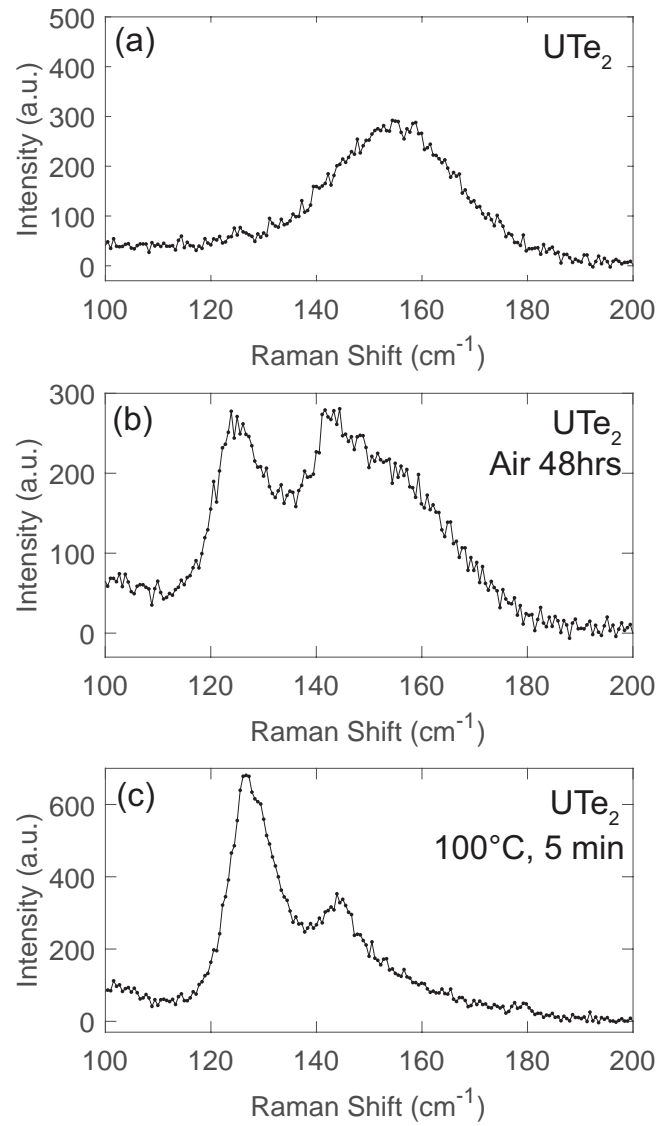


FIG. S1. Raman spectra in (a) intrinsic (b) air-exposed, and (c) heat-treated UTe_2 . For (b), the exposure time is 48hrs, and for (c), the exposure time is 5 min at 100 °C in air.

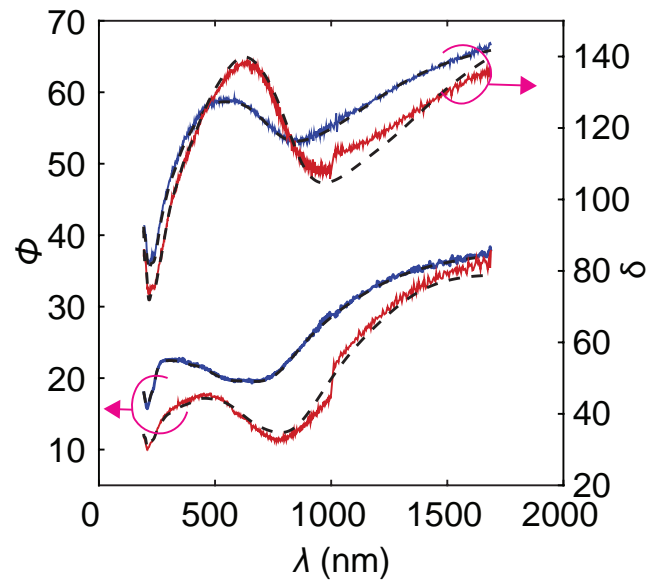


Fig. S2. Spectroscopic ellipsometry measurement for the polished UTe_2 sample (blue) and heat-treated UTe_2 sample (red). The heating condition is 100°C for 5 minutes in air. The inverse tangential component of the amplitude ratio Φ and the phase shift δ are shown at the left and right-axis, respectively. The fits to heat-treated sample using bi-layer models are shown as black dotted lines.

II. The facets of samples

We use the anisotropy in the magnetic susceptibility χ to characterize the orientations of the UTe_2 crystals. For S1, the facets include the high-symmetry axis, as shown in Fig. S3. The facet of the junctions in S1 is parallel to a and b -axis and perpendicular to c -axis. On the other hand, for S2, the facet is not parallel to any of the high-symmetry axes. Therefore, we develop the way to find the facet as described below.

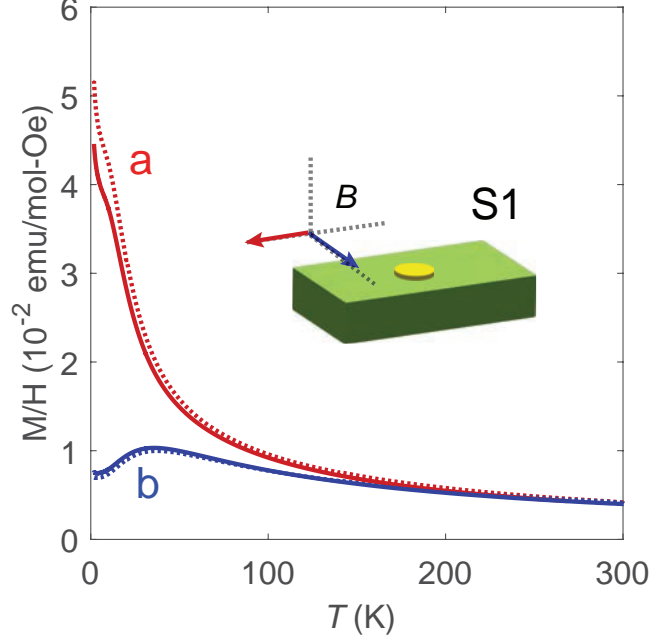


FIG. S3. The determination of the crystal orientation for S1. Two in-plane magnetic susceptibilities measured in S1 matched with χ_{aa} and χ_{bb} . Each B field direction is represented in the inset. Solid lines are our data in S1, and dotted lines are χ_{aa} and χ_{bb} adopted from S. Ran, et al. [2].

Consider the initial principal axes of coordinates x, y, z corresponds to the a, b, c axis of UTe_2 crystal structure. Then, the magnetic susceptibility tensor can be represented as the following.

$$\chi = \begin{pmatrix} \chi_{aa} & 0 & 0 \\ 0 & \chi_{bb} & 0 \\ 0 & 0 & \chi_{cc} \end{pmatrix} \quad (1)$$

where χ_{aa} , χ_{bb} , χ_{cc} are the magnetic susceptibilities in a , b , c directions when the magnetic field B is applied in a , b , c directions, respectively. Their temperature dependence is reported in S. Ran et al. [2]. When the axes are rotated around z -axis by θ , the magnetic

susceptibility in the new axes χ' can be represented as the following change of basis.

$$\chi' = \mathbf{R}_{z,\theta} \chi \mathbf{R}_{z,\theta}^T \quad (2)$$

where the rotation matrix $\mathbf{R}_{z,\theta}$

$$\mathbf{R}_{z,\theta} = \begin{pmatrix} \cos \theta & -\sin \theta & 0 \\ \sin \theta & \cos \theta & 0 \\ 0 & 0 & 1 \end{pmatrix}$$

This representation in the new coordinate can be generalized to three rotations around y , z , and x axes with the Euler's angles α , β , and γ .

$$\chi' = \mathbf{R}_{x,\gamma} \mathbf{R}_{z,\beta} \mathbf{R}_{y,\alpha} \chi \mathbf{R}_{y,\alpha}^T \mathbf{R}_{z,\beta}^T \mathbf{R}_{x,\gamma}^T \quad (3)$$

In UTe_2 , the magnetic susceptibility along b -axis, χ_{bb} has a distinctive downturn below ~ 20 K whereas χ_{aa} and χ_{cc} increase monotonically with decreasing temperature. Based on this fact, we first find the most b axis-like curve when B -field is applied in-plane, as shown in Fig. S4(e). This corresponds to b_3 in Fig. S4(c). Then, b_3 becomes the projection of the crystallographic b -axis (b_1 in Fig. S4(a) or equally b_2 in Fig. S4(b)) onto the sample facet. By fitting the magnetic susceptibility using eq. (2), we can find the projection angle $\beta = 17^\circ$ which nicely fit the experimental data as shown in Fig. S4(e). With this data, crystallographic a and c are not constrained.

Next, in order to find a and c axis, we need to fit another curve measured with in-plane B field shown in Fig. S4(d) and S4(f). This is 41° degree off from the most b -like axis, and this is expected γ . Fitting the corresponding curve using eq. (3) results in $(\alpha, \beta, \gamma) = (67^\circ, 16^\circ, 33^\circ)$. β is nicely matched with the one obtained from Fig. S4(e), indicating that this method of finding randomly oriented facets is reliable. γ is off by 8° from the expected angle measured under the microscope. This difference can come from a small misalignment in sample mounting. These fit parameters can be converted to the normal vector of the facet $\hat{n} = [0.4, 0.6, 0.7]$.

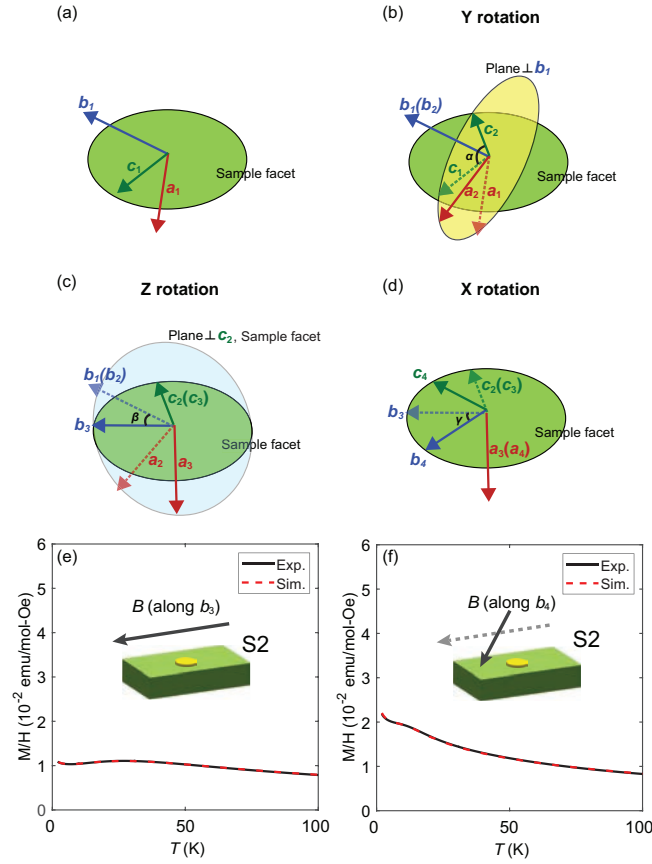


FIG. S4. The determination of the crystal orientation for S2 using YZX Euler rotations. (a) a_1, b_1, c_1 are the crystallographic a, b, c axes in UTe_2 . The green plane represents the sample facets. (b) The new coordinate system, denoted by a_2, b_2 , and c_2 , is obtained by transforming the original coordinates a_1, b_1 , and c_1 through a rotation around the Y -axis by the angle α – in this case, around the b_1 -axis. Here, α is set to ensure that c_2 lies in the sample facet. (c) The new coordinate system, denoted by a_3, b_3 , and c_3 , is obtained by transforming the original coordinates a_2, b_2 , and c_2 through a rotation around the Z -axis by the angle β . Here, β is set to ensure that b_3 lies in the sample facet. Also, a_3 becomes perpendicular to the sample facet as a result. The light blue plane represents the plane perpendicular to both c_2 and the sample facet. (d) The new coordinate system, denoted by a_4, b_4 , and c_4 , is obtained by transforming the original coordinates a_3, b_3 , and c_3 through a rotation around the X -axis by the angle γ . (e) shows the experimental data of the magnetic susceptibility and the fit of the data for the most b axis-like magnetic susceptibility in response to the in-plane B field. In YZX -rotation model, this corresponds to the case when B field is applied along b_3 axis described in (c) – In other words, $\gamma = 0$. The fit parameters are $\beta = 17^\circ$ and $\gamma = 0^\circ$. Any α gives the same fit. (f) shows the experimental data of the magnetic susceptibility and the fit of the data when B field is applied 41° off from the measurement in (e). In YZX -rotation model, this corresponds to the case when B field is applied along b_4 axis described in (d). The fit parameters are $\alpha = 67^\circ, \beta = 16^\circ, \gamma = 33^\circ$.

III. The upper critical field of samples

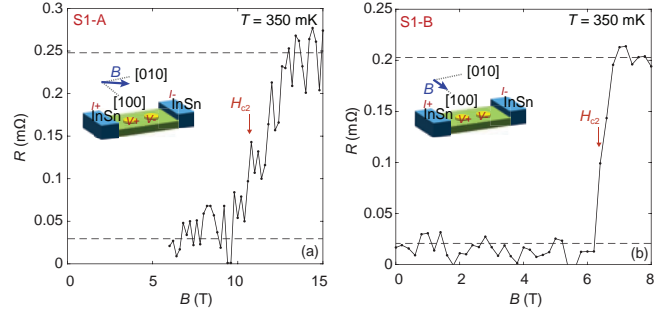


FIG. S5. (a) and (b) shows the resistance as a function of B field for S1-A and S1-B, respectively. For S1-A, B field is applied in-plane, 15° off from the b -axis. For S1-B, B field is applied in-plane along a -axis. Ohmic contacts are used as current leads and point-contacts are used as voltage leads. The dashed lines show the average values of first and last 7 data points in the curve, respectively, taken as the value for the resistance in superconducting states and normal states. H_{c2} is defined by the 50% of transitions.

For S2-A and S2-B, H_{c2} is estimated to be ~ 9 T. The B field is applied out-of-plane, which is close to $[111]$. H_{c2} along $[011]$ and $[110]$ is close to 9 T, and we expect a smooth evolution of H_{c2} between $[011]$ and $[110]$ [3].

IV. Magnetic field dependence in S1-A.

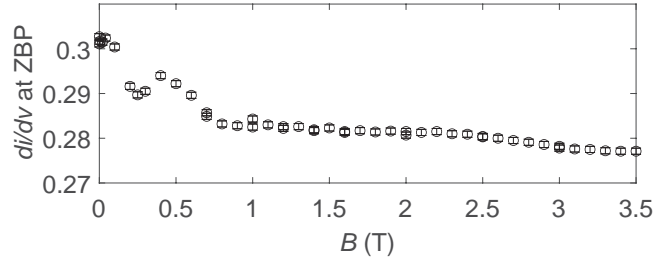


FIG. S6. Magnetic field dependence of the peak value of the zero-bias-peak (di/dv at ZBP) in S1-A.

For our junctions, whereas the ZBP ceases to exist at around T_c , it disappears earlier than $\mu_0 H_{c2}$ at around 3.5 T in response to the in-plane magnetic field. The maximum value of the ZBP has an oscillation with respect to the in-plane magnetic field, which resembles the Fraunhofer pattern shown in the Josephson junction. This observation supports the Josephson supercurrent hypothesis as the origin of the ZBP. The estimated junction area is $0.008 \mu\text{m}^2$ when the first lobe approximately ends at 0.25 T. Interestingly, it has been reported that the Josephson effect is observed with normal-metal electrodes in UBe_{13} point-contact. The origin is discussed as a proximitized normal layer or phase-slip [4, 5], and our observation may share the origin with that.

V. S2-A

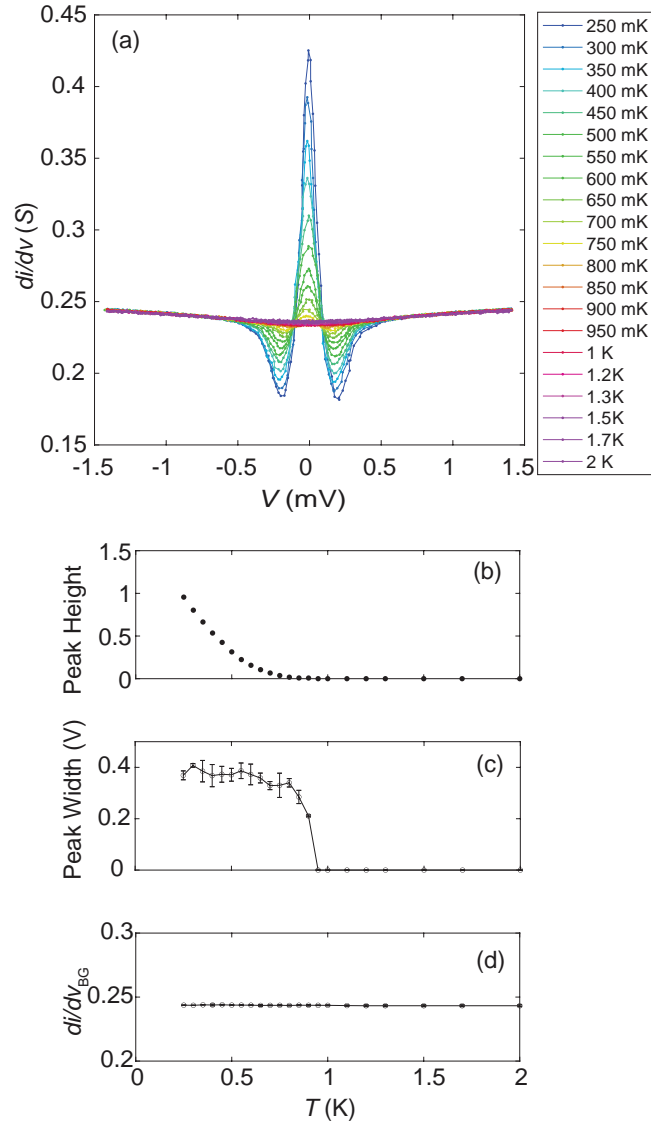


FIG. S7. Temperature dependence of the spectra in S2-A. (a) shows the temperature dependence of the raw data. (b) shows the extracted spectra peak height as a function of temperature. The peak height here is defined by the maximum value of spectra subtracted by 1 in the normalized dI/dV spectra. (c) shows the extracted peak width as a function of temperature. The peak width is defined by the distance between the dips. (d) shows the background at high bias regime. It is obtained by averaging 10 data points from each end.

VI. Theory

Within the generalized Blonder-Tinkham-Klapwijk (BTK) theory [6, 7] the conductance of a normal metal-superconductor junction is given by

$$\sigma_{\text{BTK}}(E) = \int \left(1 - \frac{1}{2} \sum_{\sigma, \sigma'} (|b_{\sigma, \sigma'}(\mathbf{k}_{\parallel}, E)|^2 - |a_{\sigma, \sigma'}(\mathbf{k}_{\parallel}, E)|^2) \right) d\mathbf{k}_{\parallel}. \quad (4)$$

where $a_{\sigma, \sigma'}(\mathbf{k}_{\parallel}, E)$ and $b_{\sigma, \sigma'}(\mathbf{k}_{\parallel}, E)$ give the probability amplitude that an incident spin- σ electron with momentum component \mathbf{k}_{\parallel} parallel to the interface and energy E is Andreev reflected as a spin- σ' hole or normal reflected as a spin- σ' electron. Our generalized BTK theory employs a number of standard simplifying assumptions [8]: the Fermi surfaces in both materials are assumed to be spherical with the same radius k_F and isotropic effective mass m^* ; we model the interface by a δ -function potential of strength $\hbar^2 k_F Z / 2m^*$; and we neglect the variation of the gap near the surface. Relaxing these assumptions may alter the quantitative values of our fit parameters but is not expected to qualitatively alter our conclusions; in particular, the topological origin of the ZBP makes this feature immune to details of the system. We performed a least-squares fit to the experimental data, using as our fitting parameters the relative strength of the different components, the overall gap amplitude Δ , the interface barrier strength Z , and the broadening parameter Γ .

The probability amplitudes in Eq. 4 also appear in the scattering wavefunctions describing the injection of a spin- σ electron ,

$$\Psi_{\sigma}(\mathbf{k}_{\parallel}, r) = \begin{cases} \psi_{e, \sigma}^{(N)} e^{ik_{\perp} r} + \sum_{\sigma'} b_{\sigma, \sigma'}(\mathbf{k}_{\parallel}, E) \psi_{e, \sigma'}^{(N)} e^{-ik_{\perp} r} + \sum_{\sigma'} a_{\sigma, \sigma'}(\mathbf{k}_{\parallel}, E) \psi_{h, \sigma'}^{(N)} e^{ik_{\perp} r} & r < 0 \\ \sum_n c_{\sigma, n}(\mathbf{k}_{\parallel}, E) \psi_{e, n}^{(S)}(k_{\perp}, \mathbf{k}_{\parallel}) e^{ik_{\perp} r} + \sum_n d_{\sigma, n}(\mathbf{k}_{\parallel}, E) \psi_{h, n}^{(S)}(-k_{\perp}, \mathbf{k}_{\parallel}) e^{-ik_{\perp} r} & r > 0 \end{cases} \quad (5)$$

where $\psi_{e(h), \sigma}^{(N)}$ is the spinor corresponding to a spin- σ electron (hole) in the normal lead, while $\psi_{e(h), n=1,2}^{(SC)}(\mathbf{k})$ describes the two electronlike (holelike) excitations in the superconductor with wavevector \mathbf{k} and energy E . The coefficients are determined from the boundary

conditions

$$\Psi_\sigma(\mathbf{k}_\parallel, r = 0^-) = \Psi_\sigma(\mathbf{k}_\parallel, r = 0^+) \quad (6)$$

$$\partial_r \Psi_\sigma(\mathbf{k}_\parallel, r = 0^-) - \partial_r \Psi_\sigma(\mathbf{k}_\parallel, r = 0^+) = k_F Z \Psi_\sigma(\mathbf{k}_\parallel, r = 0^+) \quad (7)$$

The chief difficulty in solving these equations for the coefficients in Eq. 5 is the nontrivial matrix structure of the triplet gap function $(\mathbf{d}_\mathbf{k} \cdot \hat{\sigma})i\hat{\sigma}_y$, where $\hat{\sigma}$ is the vector of Pauli matrices $\hat{\sigma}_{\mu=x,y,z}$, and $\mathbf{d}_\mathbf{k}$ is the so-called \mathbf{d} -vector. For a general triplet pairing state in UTe₂, we expect that all elements of the pairing matrix are nonzero. This implies that the electronlike and holelike spinors in general have four nonzero elements, and so the boundary conditions describe a system of eight simultaneous equations, resulting in highly complicated expressions for the conductance.

We can nevertheless make analytic progress by assuming a unitary triplet state, i.e. we restrict ourselves to pairing where $\mathbf{d}_\mathbf{k} \times \mathbf{d}_\mathbf{k}^* = 0$. In the context of UTe₂ this implies a time-reversal-symmetric state. Assuming spin-rotation invariance in the normal metal, we are then able to choose a spin-quantization axis for *each individual* \mathbf{k}_\parallel such that the \mathbf{d} -vectors at $\mathbf{k}_o = (k_\perp, \mathbf{k}_\parallel)$ and $\mathbf{k}_i = (-k_\perp, \mathbf{k}_\parallel)$ (i.e. the “outgoing” and “incoming” wavevectors in the wavefunction Ansatz Eq. 5) lie in the x - y plane, and hence involve only so-called equal-spin pairing. This reduces the 4×4 Bogoliubov-de Gennes equation to two 2×2 matrices, one for each spin orientation.

Denoting the \mathbf{d} -vectors at \mathbf{k}_o and \mathbf{k}_i in the original basis by \mathbf{d}_o and \mathbf{d}_i , respectively, we have in the rotated basis

$$\mathbf{d}'_o = \frac{d_{i,z}(\mathbf{d}_o^2 - d_{o,z}^2) - d_{o,z}((\mathbf{d}_i \cdot \mathbf{d}_o - d_{i,z}d_{o,z}))}{|\hat{\mathbf{z}} \times (\mathbf{d}_o \times \mathbf{d}_i)|} \hat{\mathbf{x}} - d_{o,z} \frac{|\mathbf{d}_o \times \mathbf{d}_i|}{|\hat{\mathbf{z}} \times (\mathbf{d}_o \times \mathbf{d}_i)|} \hat{\mathbf{y}} \quad (8)$$

$$\mathbf{d}'_i = \frac{-d_{o,z}(\mathbf{d}_i^2 - d_{i,z}^2) + d_{i,z}((\mathbf{d}_i \cdot \mathbf{d}_o - d_{i,z}d_{o,z}))}{|\hat{\mathbf{z}} \times (\mathbf{d}_o \times \mathbf{d}_i)|} \hat{\mathbf{x}} - d_{i,z} \frac{|\mathbf{d}_o \times \mathbf{d}_i|}{|\hat{\mathbf{z}} \times (\mathbf{d}_o \times \mathbf{d}_i)|} \hat{\mathbf{y}} \quad (9)$$

The pairing potential at e.g. \mathbf{k}_o is therefore transformed as

$$\mathbf{d}_o \cdot \hat{\sigma} i \hat{\sigma}_y \rightarrow \mathbf{d}'_o \cdot \hat{\sigma} i \hat{\sigma}_y = \begin{pmatrix} -d'_{o,x} + id'_{o,y} & 0 \\ 0 & d'_{o,x} + id'_{o,y} \end{pmatrix} = \begin{pmatrix} -|\mathbf{d}_o|e^{-i\varphi_o} & 0 \\ 0 & |\mathbf{d}_o|e^{i\varphi_o} \end{pmatrix} \quad (10)$$

which allows us to define a phase φ of the pairing potential.

In terms of the rotated \mathbf{d} -vectors, we can now obtain explicit expressions for the Andreev and normal reflection coefficients for the injection of a spin- s electron (with quantization axis $\mathbf{d}_o \times \mathbf{d}_i$) as

$$a_{ss}(\mathbf{k}_{\parallel}, E) = \frac{\exp(-i\phi_{o,s})u_iv_o}{(1 + \tilde{Z}^2)u_o u_i - \tilde{Z}^2 v_o v_i \exp(-is[\phi_i - \phi_o])} \quad (11)$$

$$b_{ss}(\mathbf{k}_{\parallel}, E) = \frac{\tilde{Z}(i + \tilde{Z})[v_o v_i \exp(i\phi_{i,s} - i\phi_{o,s}) - u_o u_i]}{(1 + \tilde{Z}^2)u_o u_i - \tilde{Z}^2 v_o v_i \exp(-is[\phi_i - \phi_o])} \quad (12)$$

where $\tilde{Z} = Zk_F/k_{\perp}$,

$$u_{o/i} = \sqrt{\frac{E + \Omega_{o/i}}{2E}}, \quad v_{o/i} = \sqrt{\frac{E - \Omega_{o/i}}{2E}}, \quad \Omega_{o/i} = \sqrt{E^2 - |\mathbf{d}_{o/i}|^2}, \quad (13)$$

and we can define the phases as in Eq. 10. These formulas for the reflection coefficients are essentially identical to those for an anisotropic spin-singlet superconductor [9].

Surface bound states

We can obtain the surface bound states at the bare surface (i.e. no lead) by making the analytic continuation $E \rightarrow E + i0^+$ and searching for poles of the scattering amplitudes in the limit $Z \rightarrow \infty$. For $|E| < \min\{|\mathbf{d}_i|, |\mathbf{d}_o|\}$, we find that the surface bound states are given by the solution of the equation

$$|\mathbf{d}_i||\mathbf{d}_o| - (E - i\sqrt{|\mathbf{d}_o|^2 - E^2})(E - i\sqrt{|\mathbf{d}_i|^2 - E^2}) \exp(is[\phi_i - \phi_o]) = 0 \quad (14)$$

In particular, a phase difference of π implies that $E = 0$ is a solution (i.e. a zero-energy state), whereas for a phase difference of 0 no solution is possible. In the special case where $|\mathbf{d}_i| = |\mathbf{d}_o| = \Delta$, the bound state energies are given by

$$E_{\pm} = \pm\Delta \cos((\phi_i - \phi_o)/2) \quad (15)$$

In the main text, it was claimed that the surface bound states for a gap with a dominant p_y -wave component are very similar to those obtained for a purely p_y -wave gap. To illustrate this, let us consider the surface bound states of an A_u state with $\mathbf{d}_k = ak_x\hat{\mathbf{x}} + bk_y\hat{\mathbf{y}} + ck_z\hat{\mathbf{z}}$ at the (001) and (010) surfaces. At these surfaces, the phase differences are given by

$$(010) \text{ surface: } \quad \phi_i - \phi_o = \pi - 2 \arctan \left(\frac{\sqrt{(ak_x)^2 + (ck_z)^2}}{|b|\sqrt{k_F^2 - k_x^2 - k_z^2}} \right) \quad (16)$$

$$(001) \text{ surface: } \quad \phi_i - \phi_o = -2 \arctan \left(\frac{|c|\sqrt{k_F^2 - k_x^2 - k_y^2}}{\sqrt{(ak_x)^2 + (bk_y)^2}} \right) \quad (17)$$

where we have expressed this in terms of the momentum components parallel to the interface. We see that for $|b| \gg |a|, |c|$, the phase shift at the (010) surface is close to π except very close to the edge of the projected Fermi surface; on the other hand, the phase shift for the (001) surface is close to zero except near the zone centre or along the line $k_y = 0$. This supports our argument that the phase shifts for a pairing state with dominant p_y -wave component are very similar to those for a purely p_y -wave pairing state.

To further illustrate this, we plot the bound state spectrum at the (010) and (001) surfaces in Figs. S8 and S9, respectively, comparing the case of purely p_y -wave pairing, dominant p_y -wave pairing, and isotropic pairing. As can be seen, the dominant p_y -wave pairing state has aspects of both the purely p_y -wave pairing and the isotropic pairing: surface states for all momenta within the projected Fermi surface, and a Dirac cone in the zone centre. However, the edge states of the dominant p_y -wave state are also quite similar to that for the purely p_y -wave gap: close to zero energy for the (010) surface, and also close to the gap edge for the (001) surface. For sufficiently high temperature and broadening parameter, the differences between the surface spectra for the dominant and purely p_y -wave states cannot be resolved in the tunneling conductance, and the purely p_y -wave state gives a qualitatively correct guide to the tunneling conductance.

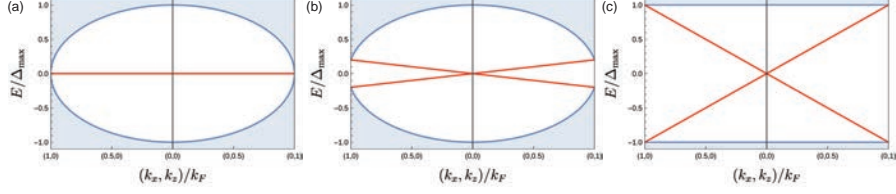


FIG. S8. Bound states at the (010) surface for (a) purely p_y -wave pairing, (b) an anisotropic A_u state with $b = 5a = 5c$, (c) an isotropic A_u state with $b = a = c$. The continuum region is shaded, while the surface bound states are shown as the red lines.

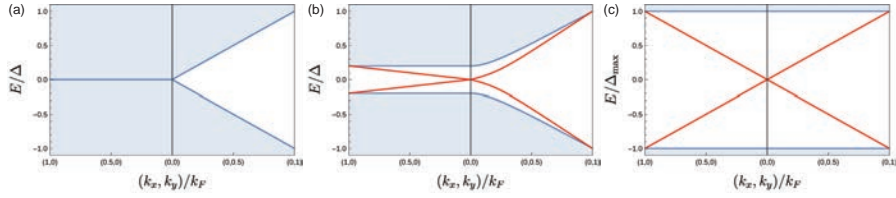


FIG. S9. Bound states at the (001) surface for (a) purely p_y -wave pairing, (b) an anisotropic A_u state with $b = 5a = 5c$, (c) an isotropic A_u state with $b = a = c$. The continuum region is shaded, while the surface bound states are shown as the red lines.

VII. BTK fits to S1-A and S1-B

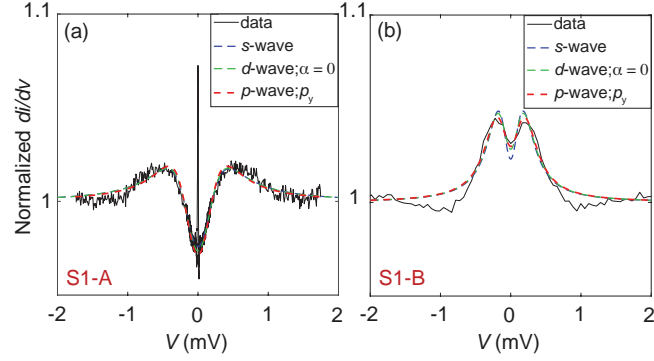


FIG. S10. BTK fits for S1-A and S1-B using s -wave, d -wave, and p -wave symmetry. To capture the gap-like feature in S1-A and S1-B, α is set to be zero in d -wave model, where $\Delta = \cos(2(\theta + \alpha))$. p_y symmetry is used for p -wave model. The fitting parameters Δ , Γ , and Z are shown in Table S1.

Sample	Symmetry	Δ (meV)	Γ (meV)	Z
S1-A	s -wave	0.22 ± 0.052	0.29 ± 0.084	0.91 ± 0.027
	d -wave	0.15 ± 0.005	0.30 ± 0.005	0.84 ± 0.013
	p -wave	0.32 ± 0.007	0.24 ± 0.005	0.63 ± 0.008
S1-B	s -wave	0.12 ± 0.008	0.14 ± 0.006	0.50 ± 0.001
	d -wave	0.18 ± 0.012	0.14 ± 0.012	0.50 ± 0.001
	p -wave	0.26 ± 0.014	0.13 ± 0.015	0.32 ± 0.02

Table S1. The fitting parameters Δ , Γ , and Z for BTK fits in Fig. S10, using s -wave, d -wave, and p -wave symmetry.

VIII. Sample Information

A. Structural parameters for junctions

Sample	Facet	Junction	Metal	Diameter	Wiring
S1	(001)	A	Ti(3 nm)/Au(150 nm)	340 μm	silver paste
		B	Ti(5 nm)/Au(150 nm)	340 μm	silver paste
S2	$\hat{n} = [0.4, 0.6, 0.7]$	A	Ti(3 nm)/Au(150 nm)	340 μm	Au wire bonding
		B	Ti(3 nm)/Au(150 nm)	340 μm	silver paste

Table S2. Facets, counterelectrodes, diameters, and wiring methods for the junctions in S1 and S2.

B. Surface topography of UTe_2 single crystals after polishing

Figure S11. shows the surface topography of referential UTe_2 samples that we polish with 0.3 μm of aluminium oxide polishing pad, which is the same method for junction fabrications in this study. In the window of 30 μm by 30 μm , RMS roughness is 3.4 nm.

C. InSn solder ohmic contact

Figure S12. shows the differential conductance taken between two InSn contacts on UTe_2 single crystals at 250 mK. $I_+(I_-)$ and $V_+(V_-)$ are shorted in the sample stage, so that the measured resistance consists of UTe_2 resistance and two independent contact resistances. The resistance stays around 86 m Ω without showing the any spectroscopic feature. Also, this value is a few orders of magnitude smaller than the junction resistance including the Au/Ti/ UTe_2 point-contact. Therefore, we can safely disregard the effects between InSn- UTe_2 contact on the spectroscopic features in our spectra

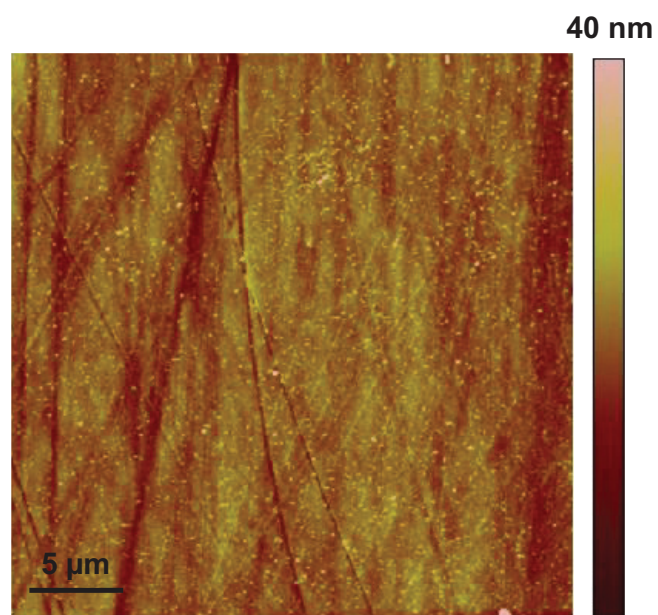


Fig. S11. Surface topography of polished surface of UTe_2 measured by atomic force microscopy.

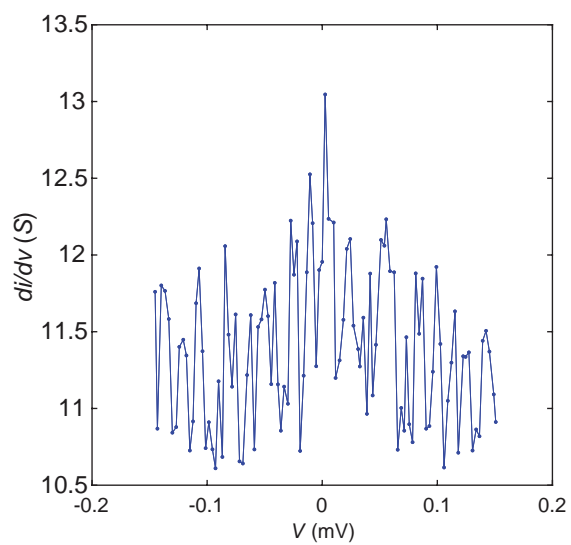


FIG. S12. The differential conductance measurement between two InSn contacts in UTe_2 single crystals.

References

- [1] Keerthana, Venimadhav, A.: TeO₂: A prospective high-k dielectric. *Phys. Status Solidi*. **18**, 2300271 (2024)
- [2] Ran, S., Eckberg, C., Ding, Q.-P., Furukawa, Y., Metz, T., Saha, S.R., Liu, I.-L., Zic, M., Kim, H., Paglione, J., Butch, N.P.: Nearly ferromagnetic spin-triplet superconductivity. *Science* **365**, 684–687 (2019)
- [3] Ran, S., Liu, I.-L., Eo, Y.S., Campbell, D.J., Neves, P.M., Fuhrman, W.T., Saha, S.R., Eckberg, C., Kim, H., Graf, D., Balakirev, F., Singleton, J., Paglione, J., Butch, N.P.: Extreme magnetic field-boosted superconductivity. *Nat. Phys.* **15**, 1250–1254 (2019)
- [4] Wolf, E.L., Han, S., Khim, Z.G., Ng, K.-W., Millis, A.J., Smith, J.L., Fisk, Z.: Proximity-josephson effect (PJE) evidence for triplet pairing in UBe₁₃. *J. Appl. Phys.* **61**, 3899–3903 (1987)
- [5] Kadin, A.M.: Analysis of the proximity-induced josephson effect in superconducting-normal contacts. *Phys. Rev. B* **41**, 4072–4077 (1990)
- [6] Blonder, G.E., Tinkham, M., Klapwijk, T.M.: Transition from metallic to tunneling regimes in superconducting microconstrictions: Excess current, charge imbalance, and supercurrent conversion. *Phys. Rev. B* **25**, 4515–4532 (1982)
- [7] Tanaka, Y., Kashiwaya, S.: Theory of tunneling spectroscopy of *d*-wave superconductors. *Phys. Rev. Lett.* **74**, 3451–3454 (1995)
- [8] Daghero, D., Gonnelli, R.S.: Probing multiband superconductivity by point-contact spectroscopy. *Supercond. Sci. Technol.* **23**, 043001 (2010)
- [9] Kashiwaya, S., Tanaka, Y.: Tunnelling effects on surface bound states in unconventional superconductors. *Rep. Prog. Phys.* **63**, 1641 (2000)